



25 **Abstract**

26 PAKRP2 is an orphan kinesin in *Arabidopsis thaliana* that is thought to transport vesicles along  
27 phragmoplast microtubules for cell plate formation. Here, using single-molecule fluorescence  
28 microscopy, we show that PAKRP2 exhibits processive plus-end-directed motility on single  
29 microtubules as individual homodimers despite having an exceptionally long (32 residues) neck  
30 linker. Furthermore, using high-resolution nanoparticle tracking to visualize motor stepping  
31 dynamics, we find that PAKRP2 achieves processivity via a noncanonical stepping mechanism  
32 that includes small step sizes and frequent lateral steps to adjacent protofilaments. We propose  
33 that the small steps sizes are due to a transient intermediate step that involves a prolonged  
34 diffusional search of the tethered head due to its long neck linker. Despite this different stepping  
35 behavior, ATP is tightly coupled to each 8-nm step. Collectively, this study reveals PAKRP2 as  
36 the first orphan kinesin to demonstrate processive motility and broadens our understanding of the  
37 diverse kinesin stepping mechanisms.

38

39

40

41

42

43

44

45

46

47

48

49

## 50 INTRODUCTION

51 Kinesins constitute a diverse superfamily of ATP-dependent, microtubule-based motor proteins  
52 that are known to participate in a variety of intracellular processes, such as microtubule  
53 organization and dynamics (1–5) and transport of cellular cargos (6, 7). Previous studies have  
54 revealed that some kinesins can move on microtubules by taking many consecutive steps before  
55 falling off, allowing them to transport organelles and protein complexes long distances (7–9). A  
56 specific example of cellular cargo transport occurs exclusively in plant cell division, which requires  
57 the construction of a cell plate at the division site. Plant kinesins hauling cell plate material walk  
58 on a microtubule-based structure called the phragmoplast, whose plus-ends are located at the  
59 developing cell wall (10, 11). In the model plant organism *Arabidopsis thaliana*, the phragmoplast-  
60 associated kinesin PAKRP2 is believed to transport Golgi vesicles to the phragmoplast midzone  
61 (12).

62 On the basis of phylogenetic analysis of the motor domains, the kinesin superfamily is  
63 divided into 14 subfamilies (kinesin-1 through kinesin-14) and an “orphan” (or ungrouped) family  
64 (13). PAKRP2 falls into the orphan family due to divergent structural features, such as a mutation  
65 in the conserved nucleotide binding site (12, 14). To date, no processive orphan kinesin has been  
66 reported, and many of the characterized orphan kinesins have mutations in the conserved  
67 residues essential for motility (15–17). Based on our current knowledge, PAKRP2’s predicted  
68 function of long-distance vesicle transport is contradictory to its classification as an orphan  
69 kinesin, but no investigation of its motility has ever been done. While processive motility isn’t  
70 necessarily required for organelle transport (18), it is a conserved feature of the prototypical  
71 transport kinesins, such as kinesin-1 and kinesin-2 (19, 20). Currently, it is not known if PAKRP2  
72 is intrinsically processive or achieves transport of cargo via clustering of several diffusive motors  
73 (18, 21) or a non-motor microtubule binding domain that enhances the microtubule affinity of the  
74 motor domain via tethering (22, 23).

75           In this study, using a combination of single-molecule fluorescence microscopy, dark-field  
76 nanoparticle tracking, and solution ATPase assays, we show that PAKRP2 is an inherently  
77 processive kinesin and surprisingly, does not exhibit typical hand-over-hand stepping behavior on  
78 a single protofilament. Close examination of the PAKRP2 sequence revealed that it contains a  
79 long neck linker that contributes to its processive behavior and does not adversely affect the motor  
80 coupling. Overall, this study provides the first glimpse at the motility of an orphan kinesin and  
81 broadens current understanding of how kinesin structure and processivity are correlated.

82

## 83 **MATERIALS AND METHODS**

### 84 **Molecular cloning, protein expression and purification**

85 The full-length cDNA of PAKRP2 was codon-optimized for protein expression in *E. coli* and  
86 synthesized as two gBlocks (IDT). The construct, containing a C-terminal His-Tag, was integrated  
87 in a modified pET17b vector via isothermal assembly and verified by DNA sequencing. All of the  
88 truncation constructs were designed for this study except for K560AviC, which was created and  
89 characterized previously (24). For protein expression, plasmids were transformed into the BL21  
90 Rosetta (DE3) competent cells (Novagen). Cells were grown at 37 °C in TPM (containing 20g  
91 tryptone, 15g yeast extract, 8g NaCl, 2g Na<sub>2</sub>HPO<sub>4</sub> and 1g KH<sub>2</sub>PO<sub>4</sub> per 1 liter) supplemented with  
92 50 µg/ml ampicillin and 30 µg/ml chloramphenicol. Expression was induced by cold shock on ice  
93 at OD<sub>600</sub> = 0.8-1 with 0.1 mM IPTG, and incubation was continued for additional 14-17 hours at  
94 20 °C. Cell pellets were harvested by centrifugation at 5,500 x g for 10 minutes using a S-5.1 rotor  
95 (Beckman Coulter) and stored at -80 °C prior to cell lysis.

96           To purify the His-tagged PAKRP2 and kinesin-1 chimera motors, cell pellets were re-  
97 suspended in the lysis buffer (50 mM sodium phosphate buffer, pH 7.2, 250 mM NaCl, 1 mM  
98 MgCl<sub>2</sub>, 0.5 mM ATP, 10 mM β-mercaptoethanol, 20 mM imidazole, and 1 µg/ml Leupeptin, 1  
99 µg/ml Pepstatin, 1 mM PMSF and 5 % glycerol), and lysed via sonication (Branson Sonifier 450).



100 The cell lysate was then centrifuged at 21,000 x g for 35 minutes using a Ti-75 rotor (Beckman  
101 Coulter). The supernatant was incubated with Talon beads (Clontech) by end-to-end mixing at 4  
102 °C for 1 hour. The protein/beads slurry was then applied to a Poly-Prep column (Bio-Rad) and  
103 washed twice with 10 column volumes of wash buffer (50 mM sodium phosphate buffer, pH 7.2,  
104 250 mM NaCl, 1 mM MgCl<sub>2</sub>, 0.1 mM ATP, 10 mM β-mercaptoethanol, 20 mM imidazole, and 1  
105 μg/ml Leupeptin, 1 μg/ml Pepstatin, 1 mM PMSF and 5% glycerol). The protein was eluted with  
106 5 column volumes of elution buffer (50 mM sodium phosphate buffer, pH 7.2, 250 mM NaCl, 1  
107 mM MgCl<sub>2</sub>, 0.5 mM ATP, 10 mM β-mercaptoethanol, 250 mM imidazole and 5 % glycerol). The  
108 eluted protein was buffer-exchanged with a PD-10 column into storage buffer (BRB80, 0.5 mM  
109 ATP, 100 mM KCl and 5% glycerol), flash frozen in liquid nitrogen, and stored at -80 °C.

110

### 111 **Polarity-marked microtubules**

112 To make polarity-marked GMPCPP microtubules, a dim bovine tubulin mix (containing 17 μM  
113 unlabeled tubulin, 17 μM biotinylated tubulin, and 0.8 μM HiLyte 647-tubulin) was first incubated  
114 in BRB80 with 0.5 mM GMPCPP (Jena Bioscience) at 37° C overnight to make dim microtubules,  
115 and then centrifuged at 250,000 x g for 7 minutes at 37° C in a TLA100 rotor (Beckman Coulter).  
116 The pellet was re-suspended in a bright bovine tubulin mix (containing 7.5 μM unlabeled tubulin,  
117 4 μM HiLyte 647-tubulin, and 15 μM NEM-tubulin) in BRB80 with 2 mM GMPCPP and incubated  
118 at 37° C for additional 15 minutes to cap the plus-end of the dim microtubules. The resulting  
119 polarity-marked track microtubules were pelleted at 20,000 x g for 7 minutes at 37° C in the  
120 TLA100 rotor (Beckman Coulter), and finally re-suspended in BRB80 with 40 μM taxol.

121

### 122 **Total internal reflection fluorescence (TIRF) microscopy**

123 All time-lapse imaging assays were performed at room temperature (22-23 °C) using the Axio  
124 Observer Z1 objective-type TIRF microscope (Zeiss) equipped with a 100x 1.46 NA oil-immersion

125 objective and a back-thinned electron multiplier CCD camera (Photometrics). All microscope  
126 coverslips were functionalized with biotin-PEG as previously described (25) to reduce nonspecific  
127 surface absorption of molecules. All time-lapse imaging experiments in this study used flow  
128 chambers that were made by attaching a coverslip to a microscope glass slide by double-sided  
129 tape.

130

### 131 **Single-molecule motility assay**

132 For single-molecule motility experiments, the chamber was perfused with 0.5 mg/ml Streptavidin  
133 to immobilize the taxol-stabilized polarity-marked HiLyte-647/Biotin-labeled microtubules. After  
134 removing unbound microtubules by washing the chamber with five-chamber volumes of BRB12  
135 supplemented with 20  $\mu$ M taxol, the chamber was perfused with a BRB80-based (or BRB50 for  
136 Kin1\_NLswap) motility mixture containing diluted motors, 1 mM ATP, 25  $\mu$ M taxol, 1.3 mg/ml  
137 casein and an oxygen scavenger system based on glucose oxidase/catalase (26). Time-lapse  
138 image sequences were recorded at 1 frame per 2 seconds with an exposure time of 200 ms for a  
139 duration of up to 10 minutes. Kymographs were generated and analyzed in ImageJ (NIH) for  
140 obtaining the velocity and run length information of individual PAKRP2 motors. Reported  
141 velocities are the peak of a Gaussian fit to the data, and associated errors are the standard  
142 deviations (SD). Characteristic run lengths were calculated by fitting an exponential cumulative  
143 distribution function to the data, and creating a bootstrap distribution to find the mean ( $n = 5000$ ).  
144 The mean was then corrected for filament length using the procedure outlined in (27), where the  
145 characteristic filament length is the average length of all microtubules used in the analysis.  
146 Reported errors are the 95% confidence intervals (CI) of the bootstrap distributions.

147

### 148 **Single-molecule photobleaching assay**

149 For single-molecule photobleaching assays, PAKRP2 molecules were immobilized, in the  
150 absence of ATP, on taxol-stabilized polarity-marked HiLyte-647/Biotin-labeled microtubules in  
151 BRB80 with 20  $\mu$ M taxol and 1.3 mg/ml casein. Time-lapse image sequences were continuously  
152 recorded with an exposure time of 100 ms until the field of view was completely bleached of  
153 fluorescence signal. The number of photobleaching steps of individual PAKRP2 motors was  
154 obtained by tracking the fluorescence intensity in ImageJ (NIH).

155

### 156 **Total internal reflection dark-field microscopy assays**

157 For single-molecule tracking experiments, we used a custom-built total internal reflection dark-  
158 field microscope as previously described (28). All experiments were carried out at 22-23 °C.  
159 PAKRP2 motors were prepared with a biotinylated C-terminal Avitag or biotinylated GFP binding  
160 protein (29), and mixed with 30-nm diameter, Streptavidin-coated gold nanoparticles. The motor  
161 was added to the gold particles at the lowest molar ratio that produced landing events (4:1 for  
162 PAKRP2 and 3:1 for K560AviC). Taxol-stabilized GDP microtubules were attached to the glass  
163 coverslip via a kinesin rigor mutant as previously described (24). High-resolution position vs. time  
164 traces were obtained from 100 frame/s (or 1000 frame/s for kinesin-1) movies by fitting the point  
165 spread function with a 2D Gaussian using Fiesta software (30). The x and y trajectories were  
166 rotated to minimize the standard deviation in the x-direction, resulting in a y-axis that is aligned  
167 with the microtubule axis.

### 168 **Step size determination**

169 The on-axis step sizes were determined by a t-test algorithm (31), for the y-displacement vs time  
170 traces. Only the traces with a standard deviation of < 3 nm from the step plateau were chosen for  
171 analysis. All reported step sizes are the mean  $\pm$  standard deviation of a single Gaussian fit to the  
172 forward steps.

## 173 **ATPase Assay**

174 ATPase assays were carried out by an enzyme-coupled assay protocol adapted from a previous  
175 study (32). Assays used 25 nM active dimeric PAKRP2(560), and 5 nM active dimeric  
176 Kin1\_NLswap, where activity was determined by assessing exchange of mantADP, as previously  
177 described (33). Hydrolysis rates at each microtubule concentration (GDP taxol-stabilized) were  
178 estimated by a linear fit to steady-state absorbance decreases at 340 nm, as previously described  
179 (33). The  $k_{cat}$  and  $K_M$  were determined by performing a least-squares fit of the ATPase vs. tubulin  
180 concentration curve to the Michaelis-Menten equation.

## 181 **RESULTS**

### 182 **PAKRP2 is a Processive Kinesin with a Long Neck Linker**

183 PAKRP2 consists of an N-terminal motor domain followed by a neck linker, a coiled-coil central  
184 stalk, and an uncharacterized C-terminal tail. Based on previous studies that show that the neck  
185 linker is an important component of kinesin processivity (34), and the fact that PAKRP2 is an  
186 orphan kinesin (14, 35), we first wanted to determine if there were any structural divergences in  
187 the neck linker region. Two coiled-coil prediction programs, COILs (36) and MARCOIL (37), both  
188 placed the likely start of the alpha-7 helix between residues 394 and 407 (Fig. 1 A and B).  
189 Examination of the sequence within that range places the first logical heptad repeat of the coiled-  
190 coil domain at residue 397, a hydrophobic methionine, followed by negatively charged aspartic  
191 and glutamic acids (Fig. 1 C). Thus, we conclude that the neck linker of PAKRP2 contains 32  
192 residues, considerably longer than the neck linkers of other kinesins, which typically contain 14-  
193 18 residues (38).

194 Several studies on kinesin-1 and kinesin-2 demonstrate that increasing the neck linker  
195 length can lead to disruptions in the stepping mechanism, such as a decrease in run length or an  
196 increase in futile ATP hydrolysis cycles (39–42). To determine whether PAKRP2 is a processive

197 microtubule motor, we engineered PAKRP2(FL), a recombinant full-length PAKRP2 with a C-  
198 terminal GFP (Fig. 2 *A* and *B*). We used a single-molecule motility assay to visualize the  
199 movement of PAKRP2(FL) on polarity-marked microtubules (Fig. 2 *C* and *D*; Supplementary  
200 Movies 1 and 2). The assay showed that individual PAKRP2(FL) molecules moved processively  
201 toward microtubule plus-ends with a mean velocity of  $65 \pm 16 \text{ nm s}^{-1}$  (mean  $\pm$  SD,  $n = 271$ ; Fig. 2  
202 *E*) and a run length of  $3.56 \pm 0.27 \mu\text{m}$  (mean  $\pm$  95% CI,  $n = 271$ , Fig. 2 *F*). The reported run  
203 lengths and the associated error are the mean and 95% confidence intervals of the bootstrap  
204 distribution. It is well established that nonprocessive kinesin motors can achieve processive  
205 motility by clustering to form multi-motor ensembles (18, 21). We thus performed single-molecule  
206 photobleaching to determine the oligomerization of PAKRP2(FL). Similar to other dimeric kinesins  
207 (18), PAKRP2(FL) was predominantly photobleached in one or two steps (Fig. S1, *A* and *B*).  
208 These results show that PAKRP2(FL) contains the ability to exhibit processive plus-end-directed  
209 motility on single microtubules as a homodimer.

210         Some kinesins are known to achieve processive motility or to gain enhanced processivity  
211 via non-motor microtubule-binding domains (22, 23, 43). To test whether PAKRP2 processivity  
212 depends on any domain beyond the head and neck linker domains, we made two additional  
213 constructs: PAKRP2(560), a truncation of the full-length at residue 560, and PAKRP2(LZ), a  
214 minimal dimer of PAKRP2 containing the motor domain and the neck linker and dimerized through  
215 a leucine zipper (Fig. 3 *A-C*). Single-molecule photobleaching experiments confirmed that  
216 PAKRP2(560) and PAKRP2(LZ) both exist predominantly as individual homodimers (Fig. S1 *C-*  
217 *F*), and exhibited processive plus-end-directed motility on single microtubules (Fig. 3 *D*,  
218 Supplementary Movies 3 and 4). The velocities of PAKRP2(560) and PAKRP2(LZ) were within  
219 error of PAKRP2(FL) (Fig. 3 *E*, Fig. S2, *A* and *C*). Run lengths of PAKRP2(560) and PAKRP2(LZ)  
220 were determined to be  $3.35 \pm 0.29 \mu\text{m}$  ( $n = 266$ , Fig. 3 *E*, Fig. S2 *B*) and  $2.67 \pm 0.25 \mu\text{m}$  ( $n = 333$ ,  
221 Fig. 3 *E*, Fig. S2 *D*), respectively. While the PAKRP2(560) run length was within 5% of the wild

222 type run length, the more significant decrease in run length of the PAKRP2(LZ) construct could  
223 indicate the native coiled-coils play a role in motility. Overall, these data show that PAKRP2  
224 processivity is largely encoded in the region containing the motor domain and the neck linker.

225

### 226 **PAKRP2 Frequently Moves Laterally**

227 Based on the knowledge that PAKRP2 is inherently processive despite having a long neck linker,  
228 we next investigated its stepping behavior to determine whether and how it may differ from that  
229 of kinesin-1. We attached a 30-nm gold particle to the C-terminus of PAKRP2(560) and observed  
230 the center-of-mass motion via dark-field nanoparticle tracking (Fig. 4 A) (44). Gold nanoparticle  
231 attachment did not significantly affect the motor activity, as the single-molecule velocity of  
232 nanoparticle-labeled motors on taxol-stabilized GDP microtubules was within 20% of the motors  
233 without nanoparticles in the same experimental conditions (Fig. S3). It should also be noted that  
234 the velocity of PAKRP2(560) without a conjugated gold nanoparticle on GDP microtubules was  
235 36% slower than its velocity without a conjugated gold nanoparticle on GMPCPP microtubules  
236 (Fig. S3). This suggests that PAKRP2(560) is sensitive to nucleotide-dependent structural  
237 changes of the microtubule lattice (45), which has also been observed in the motility of kinesin-1  
238 (46, 47).

239 When imaged at high resolution, PAKRP2(560) appeared to take frequent and sequential  
240 lateral steps both to the left and right (Fig. 4 B). To rule out that this behavior was due to surface  
241 binding of the gold nanoparticle or some other artifact of the assay, we used kinesin-1 with a gold  
242 nanoparticle on the C-terminus as a control (K560AviC, Fig. 4 C), since kinesin-1 has been  
243 demonstrated to walk on single protofilament unless it is navigating a roadblock (48, 49). The  
244 different lateral stepping characteristics of PAKRP2(560) with a gold nanoparticle on the C-  
245 terminus can be seen clearly when compared to K560AviC (Fig. 4 D). To quantify the lateral  
246 stepping behavior, a distribution of the lateral displacement per 40 nm of on-axis displacement

247 was generated for both motors (Fig. 4 E). The standard deviations for the Gaussian fits to the  
248 histograms of average off-axis displacements were 12.3 nm ( $n = 99$ ) and 5.1 nm ( $n = 113$ ) for  
249 PAKRP2 and kinesin-1, respectively, confirming that PAKRP2 steps laterally more than kinesin-  
250 1. Interestingly, the respective means were -1.5 nm and 0.7 nm, indicating that neither motor has  
251 a significant off-axis directional bias.

252 Canonical processive kinesins are known to take sequential 8-nm center-of-mass steps  
253 for the duration of their run lengths, due to the periodicity of tubulin binding sites on a single  
254 protofilament (50–52). Using point-spread-function fitting to the gold nanoparticle position and a  
255 t-test step-finding algorithm (Fig. 4 F), we measured an on-axis, center-of-mass step size of  $5.0$   
256  $\pm 2.0$  nm for PAKRP2(560) (mean  $\pm$  SD,  $n = 958$ , Fig. 4 G). In comparison, the kinesin-1 control  
257 displayed an on-axis, center-of-mass step size of  $8.0 \pm 3.0$  nm (mean  $\pm$  SD, Fig. S4 A and B),  
258 consistent with previous results (49, 51). Thus, PAKRP2 stepping is distinct from that of kinesin-  
259 1, in both the lateral movement and the average step size.

260

### 261 **PAKRP2 Takes Intermediate Steps**

262 To better understand the individual head dynamics during PAKRP2 stepping and to confirm the  
263 small step size seen in the center-of-mass data, we attached the gold nanoparticle to one motor  
264 domain (head) of PAKRP2(560) via an N-terminal Avi-tag (Fig. 5 A). Similar to the center-of-mass  
265 construct, the head-tagged motor stepped processively along the microtubule with clearly  
266 observable steps (Fig. 5 B). Using the t-test step-finding algorithm, we measured an average step  
267 size of  $7.6 \pm 3.4$  nm (mean  $\pm$  SD,  $n = 230$ , Fig. 5 C). This value is larger than the center-of-mass  
268 step size, as expected, but is half of the 16.4 nm expected for canonical hand-over-hand stepping  
269 (39, 53). There are two plausible explanations for a step size smaller than the distance between  
270 successive binding sites on a single protofilament: the labeled head is binding to an adjacent  
271 protofilament or the steps represent transient intermediates in which the labeled head is between

272 binding sites. For instance, Stepp *et al.* demonstrated that head-labeled kinesin-2 motors take 13-  
273 nm steps on axonemes, compared to 16.4-nm steps on single microtubules (54). This discrepancy  
274 was explained by 50% of the steps landing on an adjacent site 8.2 nm away. In contrast, high-  
275 resolution nanoparticle tracking revealed that the motor domain of kinesin-1 takes intermediate  
276 steps, or substeps, at saturating ATP conditions that result in an average step size of 8.2 nm (24).

277 In order to resolve whether the PAKRP2 motor domains are taking 8.2-nm steps to  
278 adjacent protofilaments or pausing midway through 16.4-nm steps, we measured the ATPase  
279 activity of PAKRP2. Canonical steppers are known to take one step per ATP molecule hydrolyzed,  
280 as ATP binding initiates the power stroke (55, 56). It is important to remember here that the  
281 displacement of the motor's center-of-mass is approximately half the displacement of one motor  
282 head if the second head remains bound to the microtubule. Based on the measured velocity of  
283  $40 \pm 12 \text{ nm s}^{-1}$  on GDP taxol-stabilized microtubules (Fig S3), 8.2-nm steps of the center-of-mass  
284 correspond to a stepping rate of  $4.9 \text{ s}^{-1}$  and 4.1-nm steps correspond to a stepping rate of  $9.8 \text{ s}^{-1}$ .  
285 In the ATPase assay the  $k_{\text{cat}}$  for a PAKRP2(560) dimer was  $3.5 \pm 0.6 \text{ ATP/s}$  (Fig. 5 D), which is  
286 close to the rate for 8.2 nm center-of-mass steps (Fig. 5 E) and not consistent with the motor  
287 hydrolyzing multiple ATP per step. Therefore, we conclude that PAKRP2 stepping includes an  
288 intermediate step, with the final position of the head being  $\sim 16.4 \text{ nm}$  from the starting position.  
289 This result also necessitates that PAKRP2 uses one ATP per step, despite having a long neck  
290 linker, which is contrary to previous studies on kinesin-1 in which long neck linkers lead to  
291 uncoupling of the ATPase from stepping (39, 42).

292

### 293 **PAKRP2 Neck Linker Disrupts Kinesin-1 Stepping**

294 The finding that PAKRP2 contains a long neck linker domain yet retains tight coupling  
295 between its ATPase and stepping activities raises the possibility that sequence-specific structural



296 features in its long neck linker contribute to the coupling. To test whether the PAKRP2 neck linker  
297 confers tight coupling to other motors, we designed a kinesin-1 chimera, Kin1\_NLswap, in which  
298 the native 14 residue neck linker was replaced by the 32 residue PAKRP2 neck linker (Fig. 6 A,  
299 S5 A). A photobleaching assay confirmed that this construct is a homodimer in solution (Fig. S5,  
300 B and C). From kymograph analysis (Supplementary Movie 5), the single molecule velocity of  
301 Kin1\_NLswap was  $103 \pm 20 \text{ nm s}^{-1}$  ( $n = 172$ , Fig. 6 B), and the run length was  $1.64 \pm 0.19 \mu\text{m}$  ( $n$   
302  $= 172$ , Fig. 6 C). Under identical conditions, the velocity and run length of wild-type kinesin-1 are  
303  $670 \pm 70 \text{ nm s}^{-1}$  and  $1.21 \pm 0.16 \mu\text{m}$ , respectively (44). Thus, swapping the PAKRP2 neck linker  
304 into kinesin-1 significantly disrupts the stepping rate but does not substantially alter motor  
305 processivity.

306 In principle, this slower velocity could result from either slowing of the ATPase cycle or  
307 uncoupling of the hydrolysis cycle from the stepping cycle. To test between these possible  
308 mechanisms, we measured the microtubule-stimulated ATPase of Kin1\_NLswap. The  $k_{\text{cat}}$  of the  
309 Kin1\_NLswap was  $121 \pm 7 \text{ s}^{-1}$  (Fig. S6), which is significantly higher than the center-of-mass  
310 stepping rate of  $\sim 12 \text{ s}^{-1}$ , assuming it takes 8.2-nm steps. However, even if the steps were 4.1-nm,  
311 the stepping rate of  $\sim 25 \text{ s}^{-1}$  would still be considerably lower than the ATP hydrolysis rate. Thus,  
312 replacing the kinesin-1 neck linker with the longer PAKRP2 neck linker led to uncoupling of the  
313 kinesin-1 from its stepping activity. It follows that, although PAKRP2 maintains tight  
314 mechanochemical coupling despite having a long neck linker, tight coupling results from features  
315 of the motor catalytic domain rather than specific structural features of the neck linker domain.

316

### 317 **PAKRP2 Neck Linker Enhances Its Processivity**

318 Given that the PAKRP2 neck linker greatly disrupts the stepping cycle of kinesin-1, it could also  
319 negatively impact the stepping cycle of PAKRP2. To determine if the neck linker extension affects  
320 the processivity of PAKRP2, we made a mutant, PAKRP2\_NL14, in which neck linker residues

321 beyond the first fourteen amino acids in the sequence were deleted (Fig. 6 A and S5 D). The  
322 construct was also confirmed to be a homodimer (Fig. S5, E and F). In contrast to the change in  
323 velocity resulting from swapping the neck linker into Kinesin-1, shortening the PAKRP2 neck linker  
324 did not affect the stepping rate. The velocity of PAKRP2\_NL14 on GMPCPP microtubules was  
325 determined to be  $59 \pm 19 \text{ nm s}^{-1}$  ( $n = 168$ , Fig. 6 D), within 10% of wild-type PAKRP2 (Fig. 2 E).  
326 Additionally, single-molecule motility assays showed that the neck-shortened motor maintains  
327 processivity, but the run length is decreased to  $1.96 \pm 0.27 \mu\text{m}$  ( $n = 168$ , Fig. 6 E), which is 45%  
328 less than wild-type (Supplementary Movie 6). The deleted region of the neck linker has a neutral  
329 charge, making it unlikely that the reduction in run length is due to weaker electrostatic interactions  
330 between the motor domain and the microtubule (57). Therefore, unlike in other kinesins where  
331 longer neck linkers reduce inter-head coordination leading to decreased processivity, the long  
332 neck linker of PAKRP2 contributes to its substantial processivity.

333

## 334 DISCUSSION

335 In this study, we have demonstrated that the orphan kinesin PAKRP2 is inherently processive,  
336 which sets it apart from all other characterized orphan kinesins but is consistent with its putative  
337 role in vesicle transport (12). Like other orphan kinesins (17, 58–60), PAKRP2 has a divergent  
338 nucleotide-binding motif and hydrolyzes ATP more than 10-fold slower than dimeric kinesin-1 (61,  
339 62). It also contains a 32-residue neck linker that is much longer than most other members of the  
340 kinesin superfamily (38). Despite these variations in structural features that are integral to motility  
341 (40, 63), PAKRP2 is more processive than kinesin-1, and it achieves this processivity via a  
342 noncanonical stepping mechanism that includes a long one-head-bound intermediate state and  
343 frequent lateral steps.

344 In the kinesin-1 motility cycle, ATP turnover is tightly coupled to its stepping activity (55,  
345 56, 64). This coupling is thought to be facilitated by conformational changes in the neck linker,

346 which transmits tension between the two heads (41, 42). Evidence for this tension-based  
347 mechanism can be seen in the uncoupling of the heads in kinesin-1 with neck linker insertions,  
348 where in some cases the ATP turnover rate becomes much higher than the stepping rate (39,  
349 42), and in some cases the stepping rate slows relative to wild-type (39, 40). Our study confirms  
350 this behavior in kinesin-1, as the ATP hydrolysis rate of Kin1\_NLswap is much higher than the  
351 predicted stepping rate (Fig. S6). In contrast, PAKRP2 maintains tight mechanochemical coupling  
352 despite its long neck linker (Fig. 5 *E*), suggesting that the mechanism for motor coupling is  
353 different than in other kinesins. Consistent with this, shortening the PAKRP2 neck linker had no  
354 effect on the stepping rate but significantly decreased the run length (Fig. 6 *D* and *E*). These  
355 results suggest that the PAKRP2 motor domain and long neck linker have coevolved to achieve  
356 tight mechanochemical coupling through an alternative mechanism than the one that has been  
357 determined for kinesin-1.

358 High-resolution particle tracking of PAKRP2 revealed tail displacements of 5.0 nm (Fig. 4  
359 *G*), which is considerably smaller than the 8.2-nm tubulin periodicity, and motor domain  
360 displacements of 7.6 nm (Fig. 5 *C*), which is considerably smaller than the 16.4 nm periodicity  
361 expected from a classical hand-over-hand mechanism (39, 42, 53). The small step size in the  
362 PAKRP2 head-labeled traces is characteristic of an inchworm-like stepping model whereby the  
363 two motor domains walk on adjacent protofilaments, such as the stepping observed in dynein  
364 motility (26, 65). Although dynein is capable of taking coordinated hand-over-hand steps, it has  
365 also been observed to be a stochastic stepper, wherein each head hydrolyzes ATP and moves  
366 independently of the other (26, 65). Inchworm-like stepping in this case differs from the originally  
367 proposed inchworm model in that it involves two catalytically active motor domains (66, 67), and  
368 therefore two ATP molecules are burned per 8.2 nm step. This type of stepping in dynein is  
369 facilitated by the flexibility between the two heads (68), making it a plausible mode of motion for  
370 a kinesin with a long neck linker. However, the ATPase data that show PAKRP2 burns one ATP

371 molecule per 8.2 nm step oppose this explanation for the unusual step sizes seen in PAKRP2  
372 (Fig. 5 *E*). This is not to say that PAKRP2 does not step on adjacent protofilaments, which was  
373 clearly shown in the center-of-mass data, but that the step does not end at a binding site 8.2 nm  
374 away.

375 An alternative explanation for the small PAKRP2 step sizes is that particle tracking is  
376 detecting an intermediate step (or substep) of the tethered motor head before it reaches the next  
377 binding site. A 2015 study on kinesin-1 labeled on one motor domain at saturating ATP observed  
378 8.2-nm substeps that were attributed to a transient one-head-bound state following ATP binding  
379 and preceding ATP hydrolysis (24). In the present study, detection of these intermediate states  
380 by particle tracking could be facilitated by the slow stepping rate of PAKRP2, which is ~20-fold  
381 slower than kinesin-1. Step sizes smaller than 16.4 nm have been observed before in kinesin-1  
382 mutants with long neck linkers, but they were not attributed to substeps (39). In support of a  
383 transient one-head-bound state, a recent study demonstrated that the duration of the one head-  
384 bound state can be increased by increasing the neck linker length in kinesin-1 and kinesin-2  
385 motors, an effect that may result from an increase in the area of diffusional search taken by the  
386 tethered head before binding (44). Taken together, the PAKRP2 data align best with a substep  
387 model, though the exact mechanism of this substep may be different than what is seen in kinesin-  
388 1. In canonical processive steppers, such as kinesin-1 and kinesin-2, an increase in the one head-  
389 bound state duration leads to a higher probability that the bound head detaches before the trailing  
390 head binds, and consequently, causes a reduction in processivity of the motor (44). In contrast,  
391 shortening the neck linker of PAKRP2, which presumably decreases the one-head-bound state,  
392 resulted in reduced processivity (Fig. 6 *E*).

393 Another example of a kinesin with an unusually long neck linker is Zen4, a member of the  
394 kinesin-6 family that plays a role in microtubule organization during cytokinesis (69). The neck  
395 linker of Zen4 is 75 residues long and includes a binding site for GTPase activating proteins (70),

396 but does not prevent the motor from processively stepping along microtubules (71). The crystal  
397 structure of the Zen4 motor domain in a nucleotide-free state revealed that the initial segment of  
398 the neck linker docked in a backward conformation; this conformation is thought to relieve inter-  
399 head tension and allow for more stability in the two head-bound state (71). Zen4 functions  
400 primarily in crosslinking microtubules, so the long neck linker, coupled with backward docking in  
401 the two head-bound state, could potentially allow both motor heads to remain bound for long  
402 periods of time. However, despite both motors having long neck linker domains, PAKRP2 does  
403 not contain the “arginine gate” that facilitates the backward docking of the neck linker, and it is  
404 not clear how stabilization of the two head-bound state would benefit a transport motor. Thus,  
405 parallels that can be drawn between Zen4 and PAKRP2 are limited.

406         Although long neck linkers have primarily been viewed as a disadvantage for processivity  
407 (20, 38–40), there is evidence to suggest that they are an advantage for obstacle avoidance.  
408 Kinesin-2, which contains a 17-residue neck linker, has been shown to step laterally to adjacent  
409 protofilaments (48) and to be less affected than kinesin-1 by the addition of roadblocks, such as  
410 tau protein or rigor kinesin-1 motors on the microtubule track (72, 73). These studies propose that  
411 a long neck linker makes kinesin-2 sufficiently flexible to step to many of the adjacent binding  
412 sites, and less likely to dissociate from the microtubule at a roadblock. In the cell, microtubules  
413 are decorated with microtubule-associated proteins (MAPs) that could potentially block the paths  
414 of processive motors (74–77), and so this obstacle avoidance could provide a selective advantage  
415 in maximizing transport. Given that PAKRP2 is thought to transport material on the phragmoplast  
416 microtubules, it seems likely that it encounters MAPs and side stepping would be a useful feature.  
417 As a final point, consecutive side-steps have also been observed for kinesin-8, which achieves  
418 superprocessivity despite having a long neck linker domain (23, 73, 78, 79); thus side-stepping  
419 does not necessarily correlate with decreased processivity.

420           Based on the data presented here, we propose that PAKRP2 steps via a hand-over-hand  
421 mechanism that includes a transient intermediate state in which one head is bound to the  
422 microtubule, and that the motor takes frequent lateral steps to adjacent protofilaments. We  
423 propose that this stepping behavior results from the long neck linker domain, however the tight  
424 mechanochemical coupling also suggests that the neck linker and catalytic core of the motor have  
425 coevolved to achieve processivity using a stepping mechanism that is different from the classical  
426 hand-over-hand mechanism of kinesin-1 (50, 53, 67). Further single-molecule work is needed to  
427 precisely determine how PAKRP2 achieves processive stepping and tight mechanochemical  
428 coupling despite having an extended neck linker domain. It is also not known how the long neck  
429 linker might impact the ability of PAKRP2 to generate sustained forces. From a biological  
430 perspective, there is still no direct evidence that PAKRP2 can associate with vesicle membranes  
431 and it is not clear whether intracellular transport by PAKRP2 generally results from a small  
432 population of motors or a large ensemble of motors attached to the cargo. Overall, these results  
433 add to the developing model of kinesin stepping, wherein each motor steps in a way that is  
434 optimized for its structure and role in the cell.

435

#### 436 **Acknowledgments**

437 This project was partially supported through grants from the National Science Foundation to W.Q.  
438 (1616462) and the National Institutes of Health to W.O.H. (R01GM076476). K.J.M was supported  
439 by a fellowship from the National Cancer Institute (F99CA223018).

440

#### 441 **Author Contributions**

442 W.Q conceived and supervised the study. A.G. and P.W. performed all experiments. K.J.M. built  
443 the microscope used for high-resolution tracking and assisted with experiments and analysis.  
444 A.G., W.O.H. and W.Q. wrote the manuscript with input from all authors.

445

## 446 **References**

- 447 1. Wordeman, L. 2010. How kinesin motor proteins drive mitotic spindle function: lessons  
448 from molecular assays. *Semin. Cell Dev. Biol.* 21: 260–268.
- 449 2. Fukuda, Y., A. Luchniak, E.R. Murphy, and M.L. Gupta. 2014. Spatial control of  
450 microtubule length and lifetime by opposing stabilizing and destabilizing functions of  
451 Kinesin-8. *Curr. Biol.* 24: 1826–1835.
- 452 3. Ferenz, N.P., A. Gable, and P. Wadsworth. 2010. Mitotic functions of kinesin-5. *Semin.*  
453 *Cell Dev. Biol.* 21: 255–259.
- 454 4. She, Z.-Y., and W.-X. Yang. 2017. Molecular mechanisms of kinesin-14 motors in spindle  
455 assembly and chromosome segregation. *J. Cell Sci.* 130: 2097–2110.
- 456 5. Goshima, G., and R.D. Vale. 2003. The roles of microtubule-based motor proteins in  
457 mitosis: comprehensive RNAi analysis in the *Drosophila* S2 cell line. *J. Cell Biol.* 162:  
458 1003–1016.
- 459 6. Hirokawa, N., and Y. Noda. 2008. Intracellular transport and kinesin superfamily proteins,  
460 kifs: structure, function, and dynamics. *Physiol. Rev.* 88: 1089–1118.
- 461 7. Hirokawa, N., Y. Noda, Y. Tanaka, and S. Niwa. 2009. Kinesin superfamily motor proteins  
462 and intracellular transport. *Nat. Rev. Mol. Cell Biol.* 10: 682–696.
- 463 8. Encalada, S.E., L. Szpankowski, C. Xia, and L.S.B. Goldstein. 2011. Stable kinesin and  
464 dynein assemblies drive the axonal transport of mammalian prion protein vesicles. *Cell.*  
465 144: 551–565.
- 466 9. Maday, S., A.E. Twelvetrees, A.J. Moughamian, and E.L.F. Holzbaur. 2014. Axonal  
467 transport: cargo-specific mechanisms of motility and regulation. *Neuron.* 84: 292–309.
- 468 10. de Keijzer, J., B.M. Mulder, and M.E. Janson. 2014. Microtubule networks for plant cell  
469 division. *Syst. Synth. Biol.* 8: 187–194.
- 470 11. Bajer, A. 1966. Role of phragmoplast filaments in cell-plate formation. *J. Cell Sci.* 1: 455–  
471 462.
- 472 12. Lee, Y.R., H.M. Giang, and B. Liu. 2001. A novel plant kinesin-related protein specifically  
473 associates with the phragmoplast organelles. *Plant Cell.* 13: 2427–2439.



- 474 13. Lawrence, C.J., R.K. Dawe, K.R. Christie, D.W. Cleveland, S.C. Dawson, S.A. Endow, L.S.  
475 Goldstein, H.V. Goodson, N. Hirokawa, J. Howard, R.L. Malmberg, J.R. McIntosh, H. Miki,  
476 T.J. Mitchison, Y. Okada, A.S. Reddy, W.M. Saxton, M. Schliwa, J.M. Scholey, R.D. Vale,  
477 C.E. Walczak, and L. Wordeman. 2004. A standardized kinesin nomenclature. *J. Cell Biol.*  
478 167: 19–22.
- 479 14. Shen, Z., A. Collatos, J. Bibeau, F. Furt, and L. Vidali. 2012. Phylogenetic analysis of the  
480 kinesin superfamily from *Physcomitrella*. *Front. Plant Sci.* 3: 1–19.
- 481 15. Chesarone-Cataldo, M., C. Guérin, J.H. Yu, R. Wedlich-Soldner, L. Blanchoin, and B.L.  
482 Goode. 2011. The myosin passenger protein Smy1 controls actin cable structure and  
483 dynamics by acting as a formin damper. *Dev. Cell.* 21: 217–230.
- 484 16. Matthies, H.J., R.J. Baskin, and R.S. Hawley. 2001. Orphan kinesin NOD lacks motile  
485 properties but does possess a microtubule-stimulated ATPase activity. *Mol. Biol. Cell.* 12:  
486 4000–4012.
- 487 17. Sisson, J.C., K.S. Ho, K. Suyama, and M.P. Scott. 1997. Costal2, a novel kinesin-related  
488 protein in the hedgehog signaling pathway. *Cell.* 90: 235–245.
- 489 18. Jonsson, E., M. Yamada, R.D. Vale, and G. Goshima. 2015. Clustering of a kinesin-14  
490 motor enables processive retrograde microtubule-based transport in plants. *Nat. Plants.* 1:  
491 15087.
- 492 19. Vale, R.D., T. Funatsu, D.W. Pierce, L. Romberg, Y. Harada, and T. Yanagida. 1996.  
493 Direct observation of single kinesin molecules moving along microtubules. *Nature.* 380:  
494 451–453.
- 495 20. Shastry, S., and W.O. Hancock. 2011. Interhead tension determines processivity across  
496 diverse N-terminal kinesins. *Proc. Natl. Acad. Sci. U. S. A.* 108: 16253–16258.
- 497 21. Furuta, K., A. Furuta, Y.Y. Toyoshima, M. Amino, K. Oiwa, and H. Kojima. 2013.  
498 Measuring collective transport by defined numbers of processive and nonprocessive  
499 kinesin motors. *Proc. Natl. Acad. Sci.* 110: 501–506.
- 500 22. Popchok, A.R., K.-F. Tseng, P. Wang, P.A. Karplus, X. Xiang, and W. Qiu. 2017. The  
501 mitotic kinesin-14 KlpA contains a context-dependent directionality switch. *Nat. Commun.*  
502 8: 13999.
- 503 23. Mayr, M.I., M. Storch, J. Howard, and T.U. Mayer. 2011. A non-motor microtubule binding  
504 site is essential for the high processivity and mitotic function of kinesin-8 Kif18A. *PloS One.*  
505 6: e27471.
- 506 24. Mickolajczyk, K.J., N.C. Deffenbaugh, J. Ortega Arroyo, J. Andrecka, P. Kukura, and W.O.  
507 Hancock. 2015. Kinetics of nucleotide-dependent structural transitions in the kinesin-1  
508 hydrolysis cycle. *Proc. Natl. Acad. Sci. U. S. A.* 112: E7186–E7193.
- 509 25. Bieling, P., L. Laan, H. Schek, E.L. Munteanu, L. Sandblad, M. Dogterom, D. Brunner, and  
510 T. Surrey. 2007. Reconstitution of a microtubule plus-end tracking system in vitro. *Nature.*  
511 450: 1100–1105.



- 512 26. Qiu, W., N.D. Derr, B.S. Goodman, E. Villa, D. Wu, W. Shih, and S.L. Reck-Peterson.  
513 2012. Dynein achieves processive motion using both stochastic and coordinated stepping.  
514 *Nat. Struct. Mol. Biol.* 19: 193–200.
- 515 27. Thompson, A.R., G.J. Hoeprich, and C.L. Berger. 2013. Single-Molecule Motility: Statistical  
516 Analysis and the Effects of Track Length on Quantification of Processive Motion. *Biophys.*  
517 *J.* 104: 2651–2661.
- 518 28. Chen, G.-Y., K.J. Mickolajczyk, and W.O. Hancock. 2016. The kinesin-5 chemomechanical  
519 cycle is dominated by a two-heads-bound state. *J. Biol. Chem.* 291: 20283–20294.
- 520 29. Feng, Q., K.J. Mickolajczyk, G.-Y. Chen, and W.O. Hancock. 2018. Motor reattachment  
521 kinetics play a dominant role in multimotor-driven cargo transport. *Biophys. J.* 114: 400–  
522 409.
- 523 30. Ruhnaw, F., D. Zwicker, and S. Diez. 2011. Tracking single particles and elongated  
524 filaments with nanometer precision. *Biophys. J.* 100: 2820–2828.
- 525 31. Chen, Y., N.C. Deffenbaugh, C.T. Anderson, W.O. Hancock, J. Lippincott-Schwartz, and J.  
526 Lippincott-Schwartz. 2014. Molecular counting by photobleaching in protein complexes  
527 with many subunits: best practices and application to the cellulose synthesis complex. *Mol.*  
528 *Biol. Cell.* 25: 3630–3642.
- 529 32. Huang, T.G., and D.D. Hackney. 1994. *Drosophila* kinesin minimal motor domain  
530 expressed in *Escherichia coli*. Purification and kinetic characterization. *J. Biol. Chem.* 269:  
531 16493–16501.
- 532 33. Chen, G.-Y., D.F.J. Arginteanu, and W.O. Hancock. 2015. Processivity of the kinesin-2  
533 kif3a results from rear head gating and not front head gating. *J. Biol. Chem.* 290: 10274–  
534 10294.
- 535 34. Case, R.B., S. Rice, C.L. Hart, B. Ly, and R.D. Vale. Role of the kinesin neck linker and  
536 catalytic core in microtubule-based motility. *Curr. Biol.* 10: 157–160.
- 537 35. Wickstead, B., and K. Gull. 2006. A “holistic” kinesin phylogeny reveals new kinesin  
538 families and predicts protein functions. *Mol. Biol. Cell.* 17: 1734–1743.
- 539 36. Lupas, A., M. Van Dyke, and J. Stock. 1991. Predicting coiled coils from protein  
540 sequences. *Science.* 252: 1162–1164.
- 541 37. Delorenzi, M. An HMM model for coiled-coil domains and a comparison with PSSM-based  
542 predictions. .
- 543 38. Düselder, A., C. Thiede, C.F. Schmidt, and S. Lakämper. 2012. Neck-linker length  
544 dependence of processive kinesin-5 motility. *J. Mol. Biol.* 423: 159–168.
- 545 39. Yildiz, A., M. Tomishige, A. Gennerich, and R.D. Vale. 2008. Intramolecular strain  
546 coordinates kinesin stepping behavior along microtubules. *Cell.* 134: 1030–1041.

- 547 40. Shastry, S., and W.O. Hancock. 2010. Neck linker length determines the degree of  
548 processivity in kinesin-1 and kinesin-2 motors. *Curr. Biol.* 20: 939–943.
- 549 41. Hackney, D.D., M.F. Stock, J. Moore, and R.A. Patterson. 2003. Modulation of kinesin half-  
550 site ADP release and kinetic processivity by a spacer between the head groups.  
551 *Biochemistry.* 42: 12011–12018.
- 552 42. Clancy, B.E., W.M. Behnke-Parks, J.O.L. Andreasson, S.S. Rosenfeld, and S.M. Block.  
553 2011. A universal pathway for kinesin stepping. *Nat. Struct. Mol. Biol.* 18: 1020–1027.
- 554 43. Tseng, K.-F., P. Wang, Y.-R.J. Lee, J. Bowen, A.M. Gicking, L. Guo, B. Liu, and W. Qiu.  
555 2018. The preprophase band-associated kinesin-14 OsKCH2 is a processive minus-end-  
556 directed microtubule motor. *Nat. Commun.* 9: 1067.
- 557 44. Mickolajczyk, K.J., and W.O. Hancock. 2017. Kinesin processivity is determined by a  
558 kinetic race from a vulnerable one-head-bound state. *Biophys. J.* 112: 2615–2623.
- 559 45. Yajima, H., T. Ogura, R. Nitta, Y. Okada, C. Sato, and N. Hirokawa. 2012. Conformational  
560 changes in tubulin in GMPCPP and GDP-taxol microtubules observed by cryoelectron  
561 microscopy. *J. Cell Biol.* 198: 315–322.
- 562 46. McVicker, D.P., L.R. Chrin, and C.L. Berger. 2011. The Nucleotide-binding State of  
563 Microtubules Modulates Kinesin Processivity and the Ability of Tau to Inhibit Kinesin-  
564 mediated Transport. *J. Biol. Chem.* 286: 42873–42880.
- 565 47. Vale, R.D., C.M. Coppin, F. Malik, F.J. Kull, and R.A. Milligan. 1994. Tubulin GTP  
566 hydrolysis influences the structure, mechanical properties, and kinesin-driven transport of  
567 microtubules. *J. Biol. Chem.* 269: 23769–23775.
- 568 48. Hoerich, G.J., K.J. Mickolajczyk, S.R. Nelson, W.O. Hancock, and C.L. Berger. 2017. The  
569 axonal transport motor kinesin-2 navigates microtubule obstacles via protofilament  
570 switching. *Traffic.* 18: 304–314.
- 571 49. Schneider, R., T. Korten, W.J. Walter, and S. Diez. 2015. Kinesin-1 Motors Can  
572 Circumvent Permanent Roadblocks by Side-Shifting to Neighboring Protofilaments.  
573 *Biophys. J.* 108: 2249–2257.
- 574 50. Yildiz, A., and P.R. Selvin. 2005. Fluorescence Imaging with One Nanometer Accuracy:  
575 Application to Molecular Motors. *Acc. Chem. Res.* 38: 574–582.
- 576 51. Svoboda, K., C.F. Schmidt, B.J. Schnapp, and S.M. Block. 1993. Direct observation of  
577 kinesin stepping by optical trapping interferometry. *Nature.* 365: 721–727.
- 578 52. Amos, L.A., and A. Klug. 1974. Arrangement of subunits in flagellar microtubules. *J. Cell*  
579 *Sci.* 14: 523–549.
- 580 53. Yildiz, A., M. Tomishige, R.D. Vale, and P.R. Selvin. 2004. Kinesin walks hand-over-hand.  
581 *Science.* 303: 676–678.

- 582 54. Stepp, W.L., G. Merck, F. Mueller-Planitz, and Z. Ökten. 2017. Kinesin-2 motors adapt  
583 their stepping behavior for processive transport on axonemes and microtubules. *EMBO*  
584 *Rep.* 11: 1947–1956.
- 585 55. Coy, D.L., M. Wagenbach, and J. Howard. 1999. Kinesin takes one 8-nm step for each atp  
586 that it hydrolyzes. *J. Biol. Chem.* 274: 3667–3671.
- 587 56. Schnitzer, M.J., and S.M. Block. 1997. Kinesin hydrolyses one ATP per 8-nm step. *Nature.*  
588 388: 386–390.
- 589 57. Thorn, K.S., J.A. Ubersax, and R.D. Vale. 2000. Engineering the processive run length of  
590 the kinesin motor. *J. Cell Biol.* 151: 1093–1100.
- 591 58. Hu, H., L. Hu, Z. Yu, A.E. Chasse, F. Chu, and Z. Li. 2012. An orphan kinesin in  
592 trypanosomes cooperates with a kinetoplastid-specific kinesin to maintain cell morphology  
593 by regulating subpellicular microtubules. *J. Cell Sci.* 125: 4126–4136.
- 594 59. Hiwatashi, Y., M. Obara, Y. Sato, T. Fujita, T. Murata, and M. Hasebe. 2008. Kinesins are  
595 indispensable for interdigitation of phragmoplast microtubules in the moss *Physcomitrella*  
596 *patens*. *Plant Cell.* 20: 3094–3106.
- 597 60. Lillie, S., and S. Brown. 1998. Smy1p, a kinesin-related protein that does not require  
598 microtubules. *J. Cell Biol.* 140: 873–883.
- 599 61. Jiang, W., M.F. Stock, X. Li, and D.D. Hackney. 1997. Influence of the kinesin neck domain  
600 on dimerization and atpase kinetics. *J. Biol. Chem.* 272: 7626–7632.
- 601 62. Woehlke, G., A.K. Ruby, C.L. Hart, B. Ly, N. Hom-Booher, and R.D. Vale. 1997.  
602 Microtubule interaction site of the kinesin motor. *Cell.* 90: 207–216.
- 603 63. Cross, R.A. 2016. Review: Mechanochemistry of the kinesin-1 ATPase. *Biopolymers.* 105:  
604 476–482.
- 605 64. Hua, W., E.C. Young, M.L. Fleming, and J. Gelles. 1997. Coupling of kinesin steps to ATP  
606 hydrolysis. *Nature.* 388: 390–393.
- 607 65. DeWitt, M.A., A.Y. Chang, P.A. Combs, and A. Yildiz. 2012. Cytoplasmic dynein moves  
608 through uncoordinated stepping of the AAA+ ring domains. *Science.* 335: 221–225.
- 609 66. Hua, W., J. Chung, and J. Gelles. 2002. Distinguishing inchworm and hand-over-hand  
610 processive kinesin movement by neck rotation measurements. *Science.* 295: 844–848.
- 611 67. Asbury, C.L., A.N. Fehr, and S.M. Block. 2003. Kinesin moves by an asymmetric hand-  
612 over-hand mechanism. *Science.* 302: 2130–2134.
- 613 68. Bhabha, G., G.T. Johnson, C.M. Schroeder, and R.D. Vale. 2016. How dynein moves  
614 along microtubules. *Trends Biochem. Sci.* 41: 94–105.
- 615 69. White, E.A., and M. Glotzer. 2012. Centralspindlin: at the heart of cytokinesis.  
616 *Cytoskeleton.* 69: 882–892.

- 617 70. Mishima, M., S. Kaitna, and M. Glotzer. 2002. Central spindle assembly and cytokinesis  
618 require a kinesin-like protein/rhogap complex with microtubule bundling activity. *Dev. Cell.*  
619 2: 41–54.
- 620 71. Guan, R., L. Zhang, Q.P. Su, K.J. Mickolajczyk, G.-Y. Chen, W.O. Hancock, Y. Sun, Y.  
621 Zhao, and Z. Chen. 2017. Crystal structure of Zen4 in the apo state reveals a missing  
622 conformation of kinesin. *Nat. Commun.* 8: 14951.
- 623 72. Hoeprich, G.J., A.R. Thompson, D.P. McVicker, W.O. Hancock, and C.L. Berger. 2014.  
624 Kinesin's neck-linker determines its ability to navigate obstacles on the microtubule  
625 surface. *Biophys. J.* 106: 1691–1700.
- 626 73. Bormuth, V., B. Nitzsche, F. Ruhnnow, A. Mitra, M. Storch, B. Rammner, J. Howard, and S.  
627 Diez. 2012. The highly processive kinesin-8, Kip3, switches microtubule protofilaments  
628 with a bias toward the left. *Biophys. J.* 103: L4-6.
- 629 74. Kinoshita, K., B. Habermann, and A.A. Hyman. 2002. XMAP215: a key component of the  
630 dynamic microtubule cytoskeleton. *Trends Cell Biol.* 12: 267–273.
- 631 75. Drewes, G., A. Ebnet, and E.-M. Mandelkow. 1998. MAPs, MARKs and microtubule  
632 dynamics. *Trends Biochem. Sci.* 23: 307–311.
- 633 76. Mandelkow, E., and E.-M. Mandelkow. 1995. Microtubules and microtubule-associated  
634 proteins. *Curr. Opin. Cell Biol.* 7: 72–81.
- 635 77. Permana, S., S. Hisanaga, Y. Nagatomo, J. Iida, H. Hotani, and T.J. Itoh. 2005. Truncation  
636 of the projection domain of map4 (microtubule-associated protein 4) leads to attenuation of  
637 microtubule dynamic instability. *Cell Struct. Funct.* 29: 147–157.
- 638 78. Su, X., W. Qiu, M.L. Gupta, J.B. Pereira-Leal, S.L. Reck-Peterson, and D. Pellman. 2011.  
639 Mechanisms underlying the dual-mode regulation of microtubule dynamics by Kip3/kinesin-  
640 8. *Mol. Cell.* 43: 751–763.
- 641 79. Mitra, A., F. Ruhnnow, S. Girardo, and S. Diez. 2018. Directionally biased sidestepping of  
642 Kip3/kinesin-8 is regulated by ATP waiting time and motor–microtubule interaction  
643 strength. *Proc. Natl. Acad. Sci.* 115: E7950–E7959.

644

## 645 **Figure Legends**

646 **Figure 1: PAKRP2 contains a long neck linker.** (A) The coiled-coil profiles of full-length  
647 PAKRP2 predicted by COILs (red) and MARCOIL (blue). Black arrow denotes the end of the  
648 motor domain. (B) Zoomed-in coiled-coil profiles of residues just before the coiled-coil region.  
649 Black arrow denotes the end of the motor domain. (C) Sequence of residues between 394 and  
650 414 to show first heptad repeat starting at residue 397 and ending at residue 403.

651 **Figure 2: Full-length PAKRP2 is a processive plus-end-directed kinesin.** (A) Schematic  
652 diagrams of full-length PAKRP2 and PAKRP2(FL). (B) SDS-PAGE gel of PAKRP2(FL).  
653 Arrowhead indicates the expected band of PAKRP2(FL), MW = 126 kDa. (C) Schematic diagram  
654 of the single-molecule motility assay. (D) Representative kymographs of individual PAKRP2(FL)  
655 molecules moving processively towards the plus-ends of single microtubules. Scale bars: 2  
656 minutes (vertical); 5  $\mu\text{m}$  (horizontal). (E) Velocity histogram of PAKRP2(FL). Red line corresponds  
657 to a Gaussian fit with a mean value of  $65 \pm 16 \text{ nm s}^{-1}$  ( $n = 271$ ). (F) Cumulative distribution of  
658 PAKRP2(FL) run length with a characteristic run length of  $3.56 \pm 0.27 \mu\text{m}$  ( $n = 271$ ). Black circles  
659 correspond to experimental data and the red line corresponds to an exponential cdf fit.

660 **Figure 3: PAKRP2 processivity does not require C-terminal tail or stalk domain.** (A)  
661 Schematic diagram of full-length PAKRP2, PAKRP2(560) and PAKRP2(LZ). (B) SDS-PAGE gel  
662 for PAKRP2(560). Arrowhead indicates the expected band of PAKRP2(FL). MW = 91 kDa. (C)  
663 SDS-PAGE gel for PAKRP2(LZ). Arrowhead indicates the expected band of PAKRP2(FL). MW =  
664 76 kDa. (D) Representative kymographs of individual PAKRP2(560) and PAKRP2(LZ) molecules  
665 on single microtubules. Scale bars: 2 minutes (vertical); 5  $\mu\text{m}$  (horizontal). (E) Bar graphs showing  
666 the relative velocities and run lengths of PAKRP2(FL), PAKRP2(560) and PAKRP2(LZ) with  
667 corresponding errors.

668 **Figure 4: PAKRP2 takes frequent lateral steps.** (A) Schematic diagram of the gold nanoparticle  
669 placement on the C-terminus of PAKRP2(560) (B) Sample x-y traces for PAKRP2(560), where  
670 the x-axis corresponds to the microtubule axis and the y-axis corresponds to lateral movement.  
671 (C) Schematic diagram of the gold nanoparticle placement on the C-terminus of K560AviC. (D)  
672 Sample x-y traces for PAKRP2(560), where the x-axis corresponds to the microtubule axis and  
673 the y-axis corresponds to lateral movement. (E) Off-axis distance distributions for PAKRP2(560)  
674 and K560AviC. Red and blue lines correspond to a Gaussian fit to the data. (F) A representative  
675 on-axis distance vs. time plot. Raw data is shown as blue lines and steps detected by the t-test

676 step finding algorithm are shown in black. Data was acquired at 1 mM ATP every 10 ms. (G) Step  
677 size histogram of PAKRP2(560) fit to a single Gaussian ( $n = 958$ ).

678 **Figure 5: PAKRP2 takes intermediate steps.** (A) Schematic diagram of the gold nanoparticle  
679 placement on the N-terminal motor domain of Avi-PAKRP2(560). (B) A representative on-axis  
680 distance vs. time plot. Raw data are shown as purple lines and steps detected by the t-test step  
681 finding algorithm are shown in black. Data were acquired at 1 mM ATP every 10 ms. (C) Step  
682 size histogram of Avi-PAKRP2(560) fit to a single Gaussian ( $n = 230$ ). (D) The ATPase rate per  
683 dimer for PAKRP2(560) as a function of tubulin concentration. Data correspond to the mean  $\pm$  SE  
684 ( $n = 3$  or  $5$  determinations per point). The solid line represents a fit to the Michaelis-Menten  
685 equation, giving a maximum  $k_{cat}$  of  $3.5 \pm 0.6 \text{ s}^{-1}$ . (E) Comparison of the ATP hydrolysis rate per  
686 dimer and the stepping rate per dimer assuming different step sizes. Stepping rates were  
687 calculated from the division of the center-of-mass velocity by the center-of-mass step size.

688 **Figure 6: PAKRP2 neck linker affects processivity.** (A) Schematic diagram of Kin1\_NLswap  
689 and PAKRP2\_NL14. (B) Velocity histogram of Kin1\_NLswap. Red line corresponds to a Gaussian  
690 fit with a mean of  $103 \pm 20 \text{ nm s}^{-1}$  ( $n = 172$ ). (C) Run length histogram of Kin1\_NLswap. Red line  
691 corresponds to an exponential fit with a characteristic run length of  $1.64 \pm 0.19 \mu\text{m}$  ( $n = 172$ ). (D)  
692 Velocity histogram of PAKRP2\_NL14. Blue line corresponds to a Gaussian fit with a mean of  $59$   
693  $\pm 19 \text{ nm s}^{-1}$  ( $n = 168$ ). (E) Run length histogram of PAKRP2\_NL14. Blue line corresponds to an  
694 exponential fit with a characteristic run length of  $1.96 \pm 0.27 \mu\text{m}$  ( $n = 168$ ).

695 **Figure S1: PAKRP2(FL), PAKRP2(560) and PAKRP2(LZ) form homodimers in solution.** (A)  
696 Representative photobleaching traces of individual PAKRP2(FL) molecules. (B) Photobleaching  
697 histogram of PAKRP2(FL) ( $n = 441$ ). (C) Representative photobleaching traces of individual  
698 PAKRP2(560) molecules. (D) Photobleaching histogram of PAKRP2(560) ( $n = 214$ ). (E)  
699 Representative photobleaching traces of individual PAKRP2(LZ) molecules. (F) Photobleaching  
700 histogram of PAKRP2(LZ) ( $n = 266$ ).



701 **Figure S2: PAKRP2(560) and PAKRP2(LZ) velocity and run lengths.**

702 (A) Velocity histogram of PAKRP2(560). Red line corresponds to a Gaussian fit with a mean of  
703  $61 \pm 15 \text{ nm s}^{-1}$  ( $n = 266$ ). (B) Run length histogram of PAKRP2(560). Red line corresponds to an  
704 exponential fit with a characteristic run length of  $3.35 \pm 0.29 \mu\text{m}$  ( $n = 266$ ). (C) Velocity histogram  
705 of PAKRP2(LZ). Blue line corresponds to a Gaussian fit with a mean of  $66 \pm 20 \text{ nm s}^{-1}$  ( $n = 333$ ).  
706 (D) Run length histogram of PAKRP2(LZ). Blue line corresponds to an exponential fit with a  
707 characteristic run length of  $2.67 \pm 0.25 \mu\text{m}$  ( $n = 333$ ).

708 **Figure S3: Gold nanoparticle does not affect motor activity.** Bar graphs showing the relative  
709 velocities of PAKRP2(560) on GMPCPP or taxol-stabilized GDP microtubules without gold, and  
710 on taxol-stabilized GDP microtubules with gold. The velocities are  $65 \pm 16 \text{ nm s}^{-1}$  ( $n = 271$ ),  $40 \pm$   
711  $12 \text{ nm s}^{-1}$  ( $n = 47$ ) and  $32 \pm 11 \text{ nm s}^{-1}$  ( $n = 57$ ), respectively.

712 **Figure S4: Step size determination for K560AviC.** (A) A representative on-axis distance vs.  
713 time plot. Raw data is shown as red lines and steps detected by a step finding algorithm are  
714 shown in black. Data were acquired at 1 mM ATP every 1 ms. (B) Step size histogram for  
715 K560AviC with a single Gaussian fit ( $n = 664$ ).

716 **Figure S5: PAKRP2\_NL14 and Kin1\_NLswap both form individual homodimers in solution.**

717 (A) SDS-PAGE gel of Kin1\_NLswap. Arrowhead indicates the expected band of Kin1\_NLswap.  
718 MW = 75 kDa. (B) Representative photobleaching traces of individual Kin1\_NLswap molecules.  
719 (C) Photobleaching histogram for Kin1\_NLswap ( $n = 149$ ). (D) SDS-PAGE gel of PAKRP2\_NL14.  
720 Arrowhead indicates the expected band of PAKRP2\_NL14. MW = 89 kDa. (E) Representative  
721 photobleaching traces of individual PAKRP2\_NL14 molecules. (F) Photobleaching histogram for  
722 PAKRP2\_NL14 ( $n = 289$ ).

723 **Figure S6: Kin\_NLswap ATP hydrolysis and stepping rate are uncoupled.** The microtubule-  
724 stimulated ATPase rate per dimer for Kin1\_NLswap as a function of tubulin concentration. Data

725 correspond to the mean  $\pm$  SE ( $n = 3$  determinations per point). The solid line represents a fit to  
726 the Michaelis-Menten equation, giving a maximum  $k_{\text{cat}}$  of  $121 \pm 7 \text{ s}^{-1}$ .



**Figure 1**

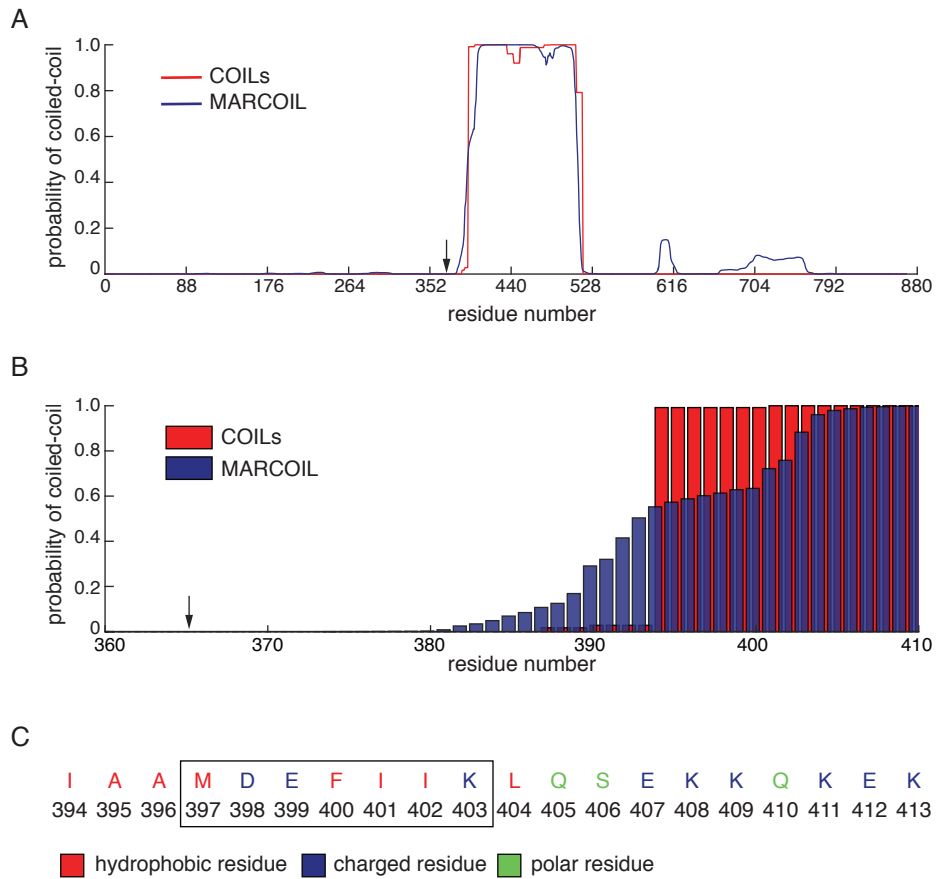


## Figure 2

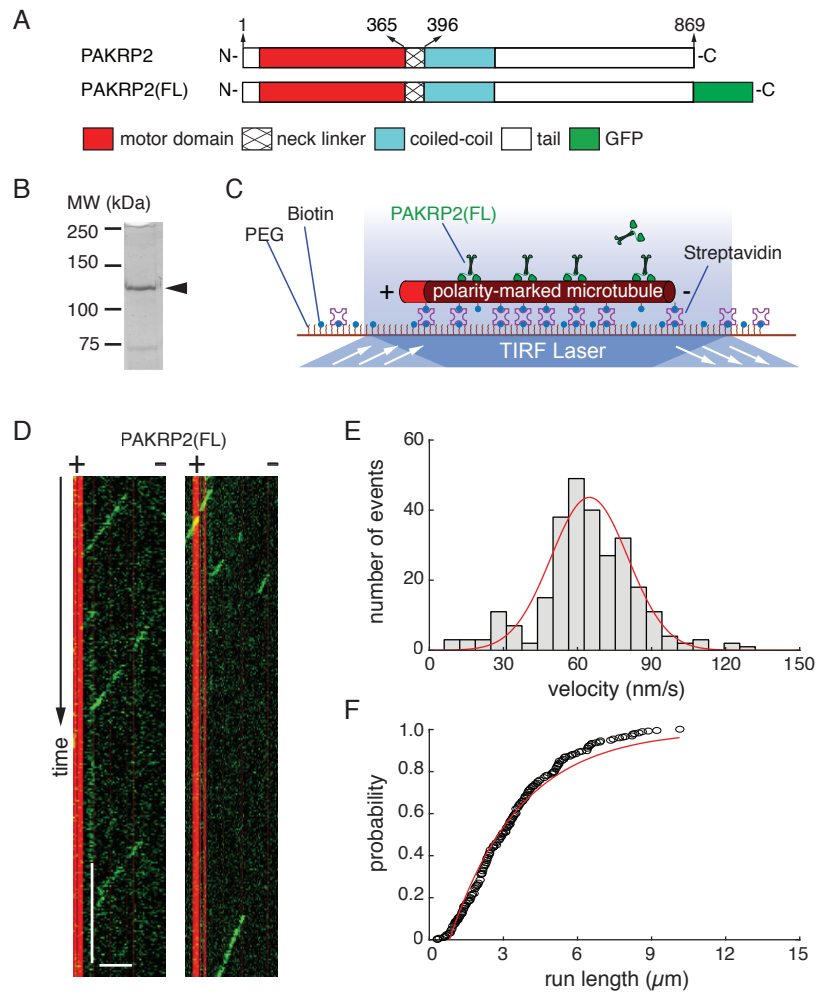


### Figure 3

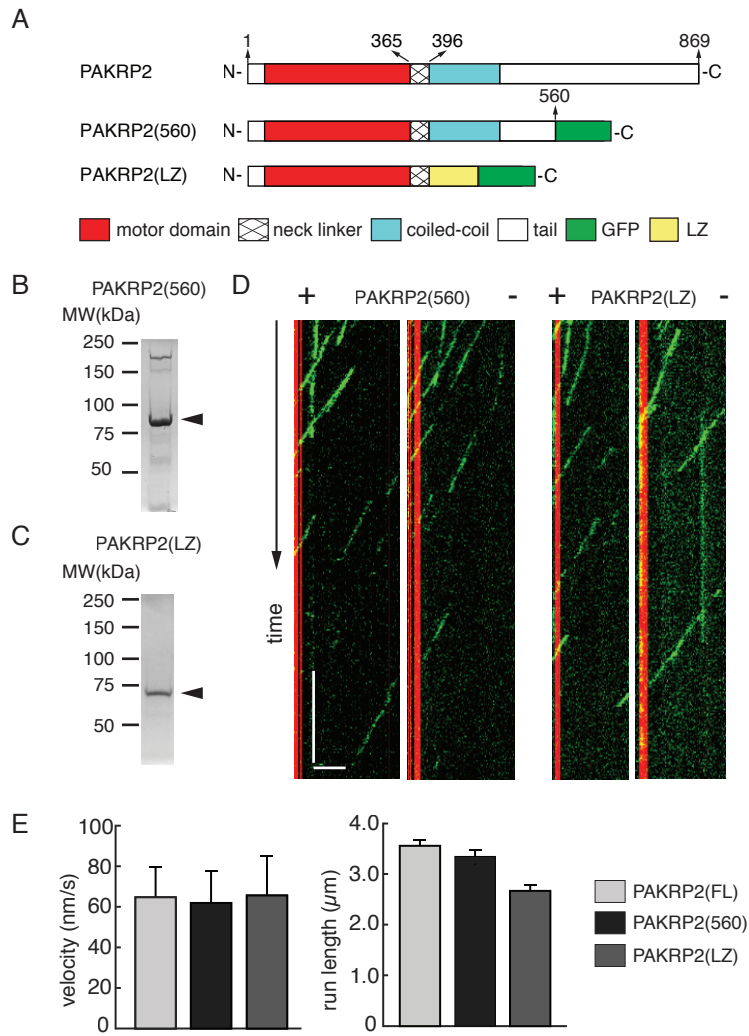


## Figure 4

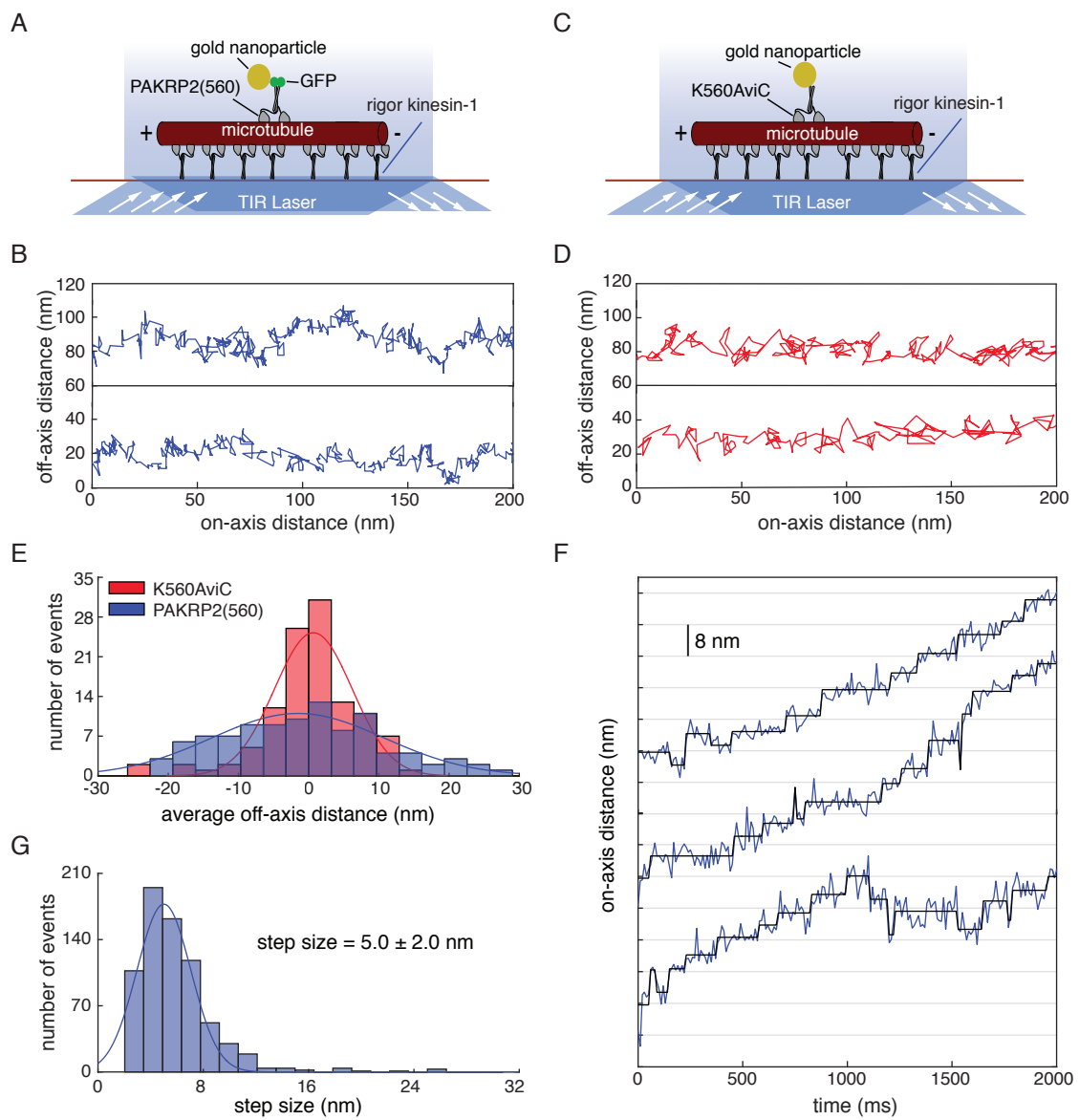


**Figure 5**

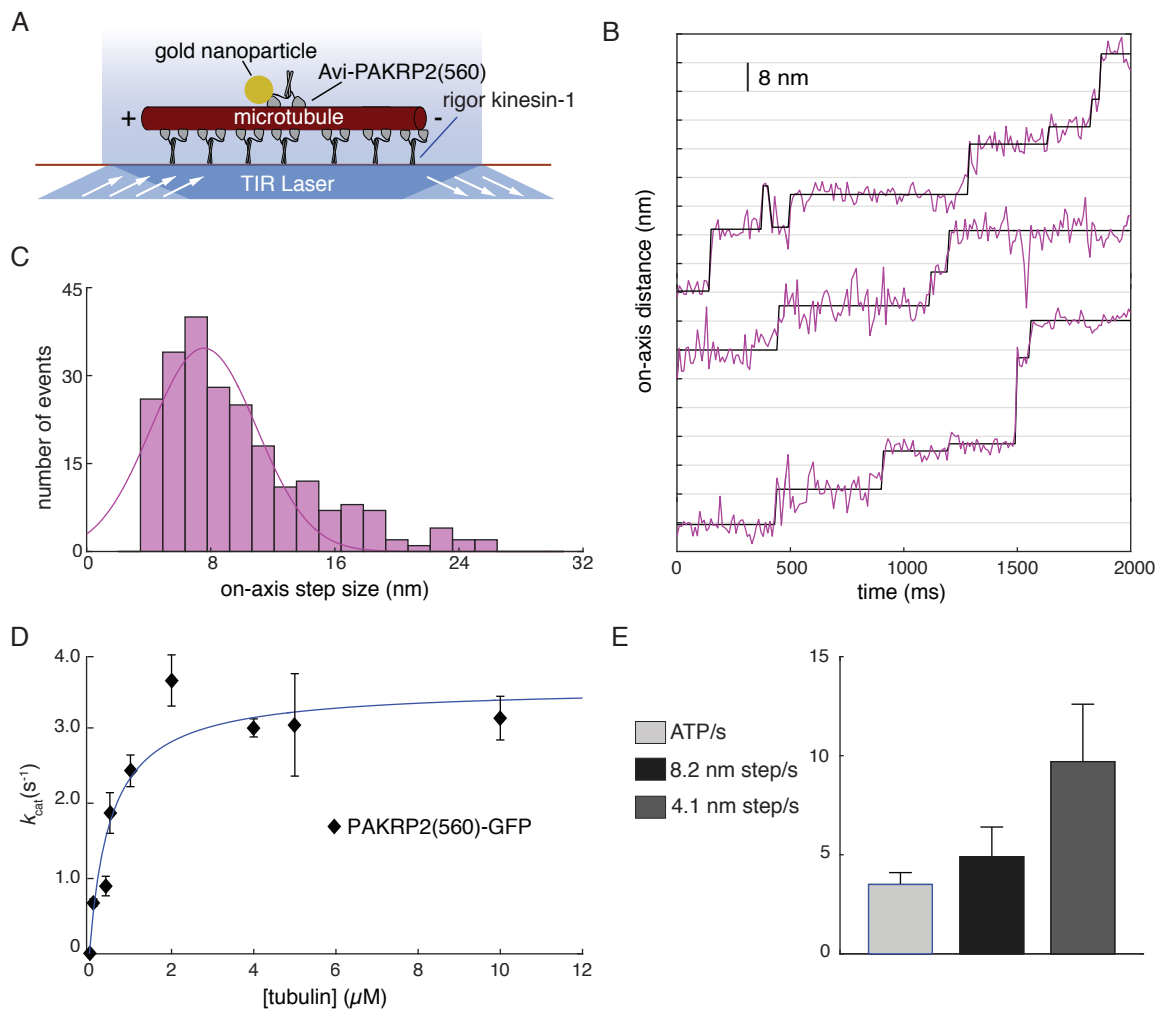


# Figure 6

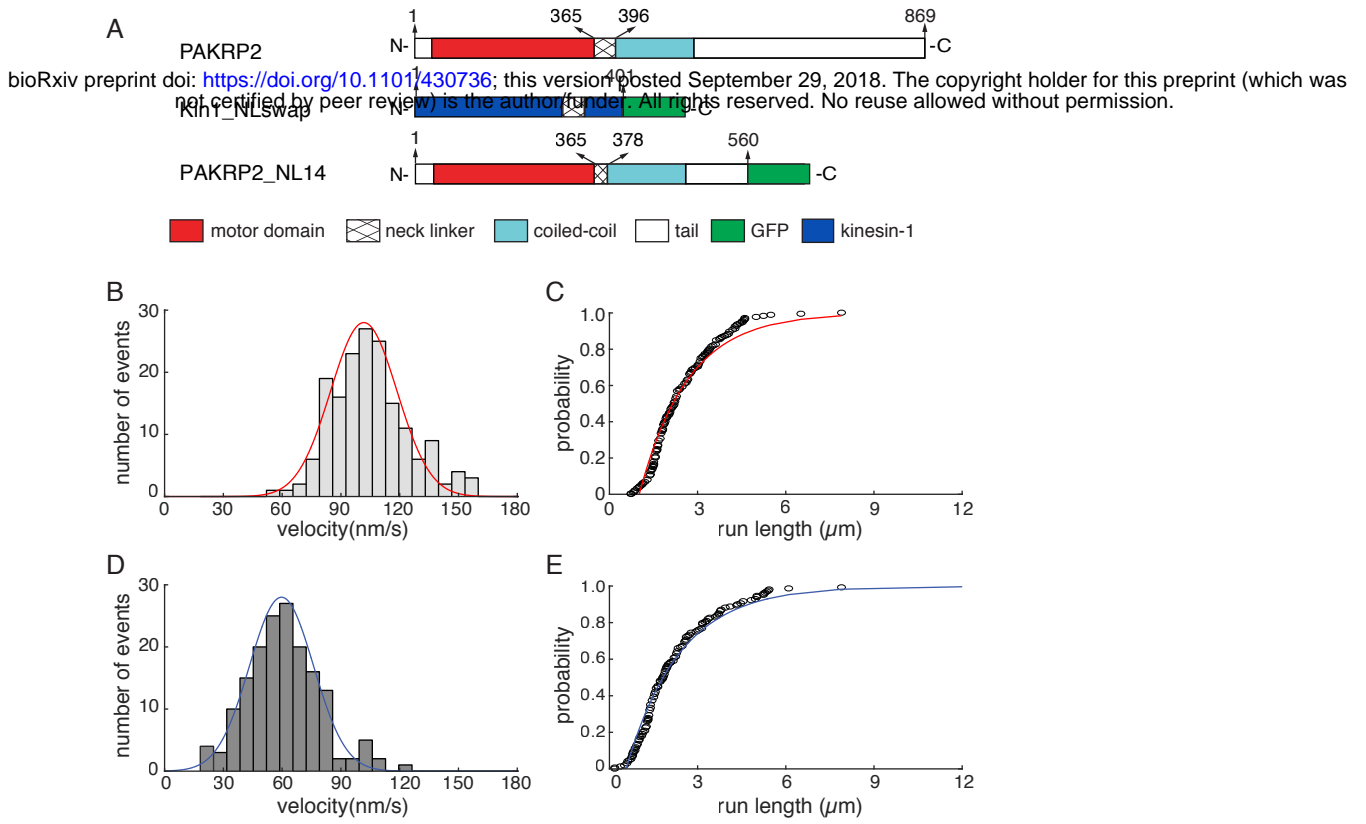


**Figure S1**

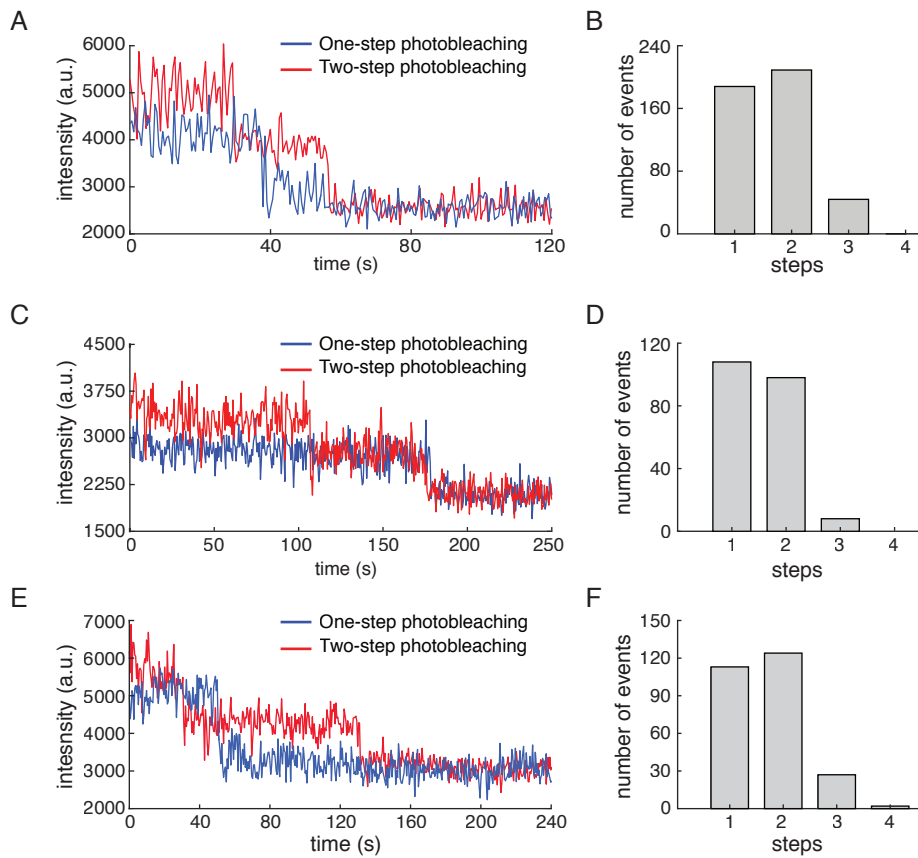


## Figure S2

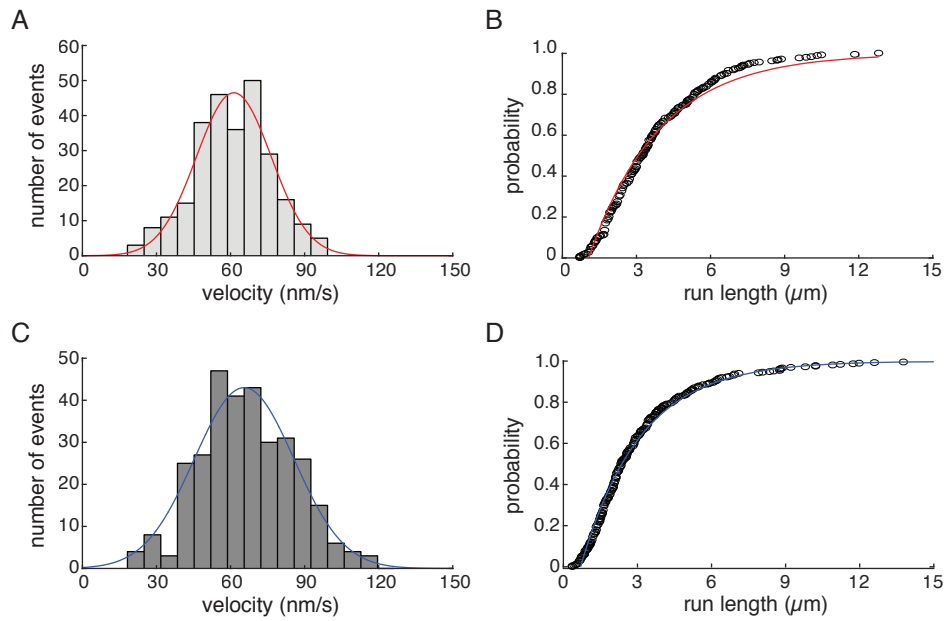




**Figure S3**

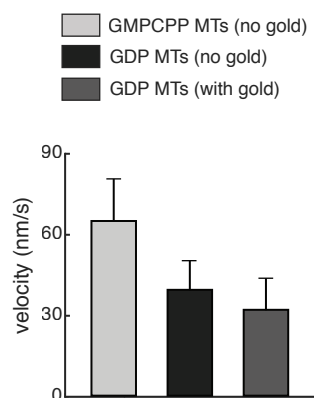
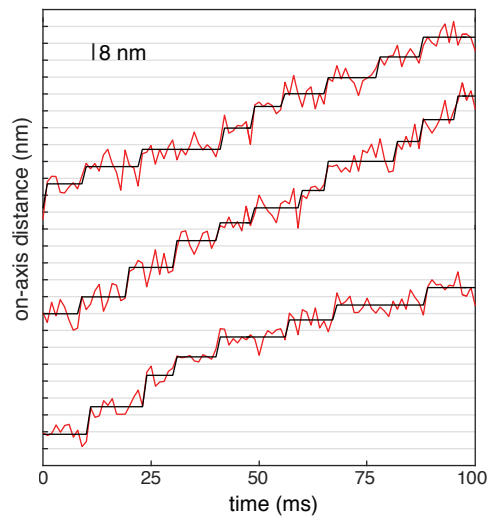


**Figure S4**

**A**



**B**

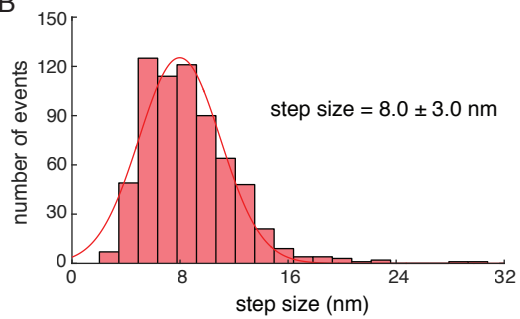


## Figure S5

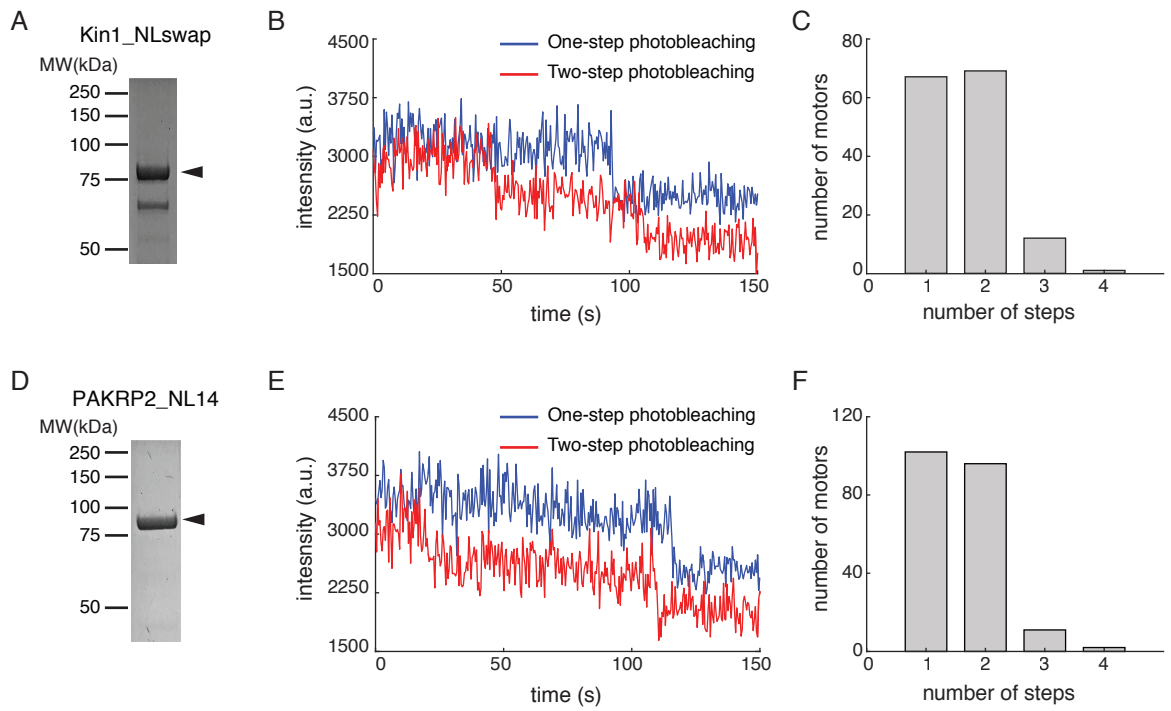


**Figure S6**

